LA-UR-15-28231 (Accepted Manuscript)

Survey of radiation belt energetic electron pitch angle distributions based on the Van Allen Probes MagEIS measurements

She, R.
Summers, D.
Ni, B.
Fennell, J. F.
Blake, J. B.
Spence, H. E.
Reeves, Geoffrey D.

To be published in: Journal of Geophysical Research: Space Physics

DOI to publisher's version: 10.1002/2015JA021724

Permalink to record: http://permalink.lanl.gov/object/view?what=info:lanl-repo/lareport/LA-UR-15-28231

Survey of radiation belt energetic electron pitch angle distributions based on the Van Allen Probes MagEIS measurements

Run Shi[1], Danny Summers[1], Binbin Ni[2], Joseph F. Fennell[3], J. Bernard Blake[3], Harlan E. Spence[4] and Geoffrey D. Reeves[5]

[1]Department of Mathematics and Statistics, Memorial University of Newfoundland, St. John's, Newfoundland, Canada

[2]Department of Space Physics, School of Electronic Information, Wuhan University, Wuhan, Hubei, China

[3]Space Science Applications Laboratory, Aerospace Corporation, El Segundo, California, USA

[4]Institute for the Study of Earth, Oceans, and Space, University of New Hampshire, Durham, New Hampshire, USA

[5]Los Alamos National Laboratory, Los Alamos, New Mexico, USA

Abstract

A statistical survey of electron pitch angle distributions (PADs) is performed based on the pitch angle resolved flux observations from the Magnetic Electron Ion Spectrometer (MagEIS) instrument on board the Van Allen Probes during the period from 1 October 2012 to 1 May 2015. By fitting the measured PADs to a $\sin^n\alpha$ form, where α is the local pitch angle and n is the power law index, we investigate the dependence of PADs on electron kinetic energy, magnetic local time (MLT), the geomagnetic Kp index and L-shell. The difference in electron PADs between the inner and outer belt is distinct. In the outer belt, the common averaged n values are less than 1.5, except for large values of the Kp index and high electron energies. The averaged n values vary considerably with MLT, with a peak in the afternoon sector and an increase with increasing L-shell. In the inner belt, the averaged n values are much larger, with a common value greater than 2. The PADs show a slight dependence on MLT, with a weak maximum at noon. A distinct region with steep PADs lies in the outer edge of the inner belt where the electron flux is relatively low. The separation between the two belts and the intensity of the geomagnetic activity together determines the variation of PADs in the inner belt. Besides being dependent on electron energy, magnetic activity and L-shell, the results show a certain dependence on MLT with higher n values on the dayside.

1. Introduction

Energetic electrons in the Earth's radiation belts are strongly influenced by the transport, energization, and loss processes which are dependent on different parameters such as electron kinetic energy, geomagnetic activity, spatial location and time. Variations of both electron flux and its pitch-angle distribution (PAD) can be essential indicators of underlying physical processes. PADs exhibit different forms in the outer and inner belt. PADs of outer belt electrons can be categorized into three types: 90° peaked, flat-top, and butterfly, which are associated with different mechanisms [*Gannon et al.*, 2007]. Butterfly distributions due to the effects of drift shell splitting and magnetopause shadowing usually occur outside 6 R_E throughout the nightside [*West et al.*, 1973; *Sibeck et al.*, 1987], while normal (90° peaked or pancake) PADs dominate the dayside magnetosphere as well as the nightside within 6R_E of Earth [*Sibeck et al.*, 1987]. *Horne et al.* [2003] investigated the evolution of electron PADs during storm time and found that at *L*~4-6, butterfly distributions formed at storm onset which could be caused by nonlocal acceleration occurring at higher (lower) latitudes. They further found that the PADs become broadly fla- top during the recovery phase. By fitting to a $\sin^n\alpha$ form, *Vampola* [1998] explored PADs using data from the Medium Electrons A instrument on the Combined Release and Radiation Effects Satellite (CRRES). *Vampola* [1998] calculated the averaged pitch-angle distribution coefficient *n* for 510keV and found a clear *L*-shell dependence but only a slight energy dependence. Applying the same method, *Gannon et al.* [2007] performed a more detailed study based on the CRRES MEA data. They examined the PADs as a function of *L*-shell and orbit number at the energies 153 keV, 510 keV and 976 keV. They concluded that the PADs on the dayside are predominately 90° peaked distributions while butterfly distributions become more common on the nightside at higher *L*-shells. *Gannon et al*. [2007] also showed that the PADs depend on MLT and magnetic activity. A further interesting finding was that the steepness of the distribution coefficient *n* at lower *L*-shell and the *L*-shell variation of the steepness is related to the plasmapause location for electron energy 153keV. In the present research, we will show that this steepness corresponds to the outer edge of inner belt and its features also depend on MLT and magnetic activity. *Gu et al*. [2011] performed a detailed statistical analysis of electron PADs near geostationary orbit (6R_E and 6.6R_E), using CRRES MEA data. The dependence on kinetic energy, MLT and the level of geomagnetic activity are quantified. The results show that the values of the distribution coefficient *n* peak within the 1200-1600 MLT sector. It is also shown that the values of *n* are smaller at lower energies and the variation of *n* is stronger for higher energies. The $\sin^n\alpha$ variation for electron PADs is a useful practical assumption in radiation belt studies [e.g., *Summers et al.*, 2009; *Summers and Shi*, 2014]. Recently, *Chen et al*. [2014] developed a new empirical model, called the relativistic electron pitch angle distribution (REPAD), to present statistical pictures of electron PADs by using Legendre polynomials to fit long-term in situ directional fluxes. This model provides higher-order information for PADs, thereby making butterfly distribution easier to identify.

PADs of the inner belt have received more attention recently thanks to the Van Allen Probes [*Zhao et al.*, 2014a, 2014b]. Based on the Magnetic Electron Ion Spectrometer (MagEIS) measurement, *Zhao et al*. [2014a] reported that a new type of PAD for hundreds of keV electrons has a minimum at 90°. Furthermore, *Zhao et al*. [2014b] identified normal and cap PADs in addition to the 90° minimum PAD at low *L* shells. They found that for ~460 keV electrons, 90° minimum PADs dominate at *L*∼1.4-1.8, while normal PADs dominate at *L*∼3.5-4; in between, 90° minimum PADs dominate during injections, while afterward minimum 90° PADs gradually disappear and normal PADs become dominant; cap PADs generally appear at *L* = 2.5-3.5 during the flux decay period following an injection.

Most recently, *Ni et al.* [2015] investigated pitch angle distributions of radiation belt ultrarelativistic (>2 MeV) electrons during storm conditions and during the long-term poststorm decay, based on the Van Allen Probes Relativistic Electron-Proton Telescope (REPT) measurements. The observed PAD coefficient *n* increases with magnetic activity in general, which suggested chorus acceleration outside the plasmasphere and electromagnetic ion cyclotron (EMIC) wave scattering inside the plasmasphere.

In the present study, by fitting the electron PADs into a $\sin^n\alpha$ form, we investigate in detail the PAD dependence on kinetic energy, MLT, magnetic activity and *L*-shell, using the MagEIS measurement onboard the Van Allen Probes during the period from 1 October 2012 to 1 May 2015. Although fitting the PADs into a $\sin^n\alpha$ form may not be fully accurate, especially for distinguishing between the normal cap PAD and the 90° minimum PAD in the inner belt, it does give us a first-order approximation of PADs for a statistical survey.

2. Data and Method of Analysis

The MagEIS (Magnetic Electron Ion Spectrometer) instrument onboard the Van Allen Probes with an apogee of ~5.8 R_E [*Mauk et al.*, 2012], provides high resolution electron flux measurements over an energy range of ~30 keV to 4 MeV [*Blake et al.*, 2013; *Spence et al.*, 2013]. Our focus in the present study will be on the MagEIS measurements made by Probe B at energies below 1 MeV. We utilize the level 3 MagEIS data set which is pitch-angle binned. Although this data set lacks resolution when analyzing the electron pitch angle distributions, it still provides a good general evolution of the PADs.

Following previous studies (*Vampola* [1998], *Gannon et al*. [2007] and *Gu et al*. [2011]), we assume the electron pitch angle distribution can be modeled by the form $\sin^n\alpha$, where α is the local pitch angle. Specifically, we use the same method as applied by *Carbary et al*. [2011]. The observed differential fluxes are fitted to the function $f = J\sin^n\alpha$, where α is the pitch angle, n is the exponent, and J is a constant. A standard least squares fit is performed, and the goodness of fit is quantified by a normalized standard deviation $\sigma_N = \sigma / \left[\max(f) - \min(f)\right]$, where σ is the usual standard deviation of the fit, max(f) is the maximum of the observed pitch angle distribution, and min(f) is the minimum. The normalized uncertainy σ_N is constrained to be less than 0.2. The data with magnetic latitudes < 85° and > 95° are excluded. The L parameter in this study is McIlwain's L-shell parameter, computed for 90° particles using the OP77Q external field and IGRF internal field.

3. Results and Discussion

Figure 1 shows the solar wind B_z component, solar wind speed V_{sw} and dynamic pressure P_{dyn}, and the Dst, Kp and AE indices during the period from 1 October 2012 to 1 May 2015. These data were obtained from the OMNI website (http://omniweb.gsfc.nasa.gov).

Examples of the electron PAD fitting are given in Figure 2. The top panels are the fittings for 100 keV electrons at the indicated four *L*-shells. The first panel shows the fitting at *L*=2.09 (inner belt). The electron flux at 90° pitch angle is slightly smaller than the values at 74° and 106°, which is consistent with the 90° minimum PAD reported by *Zhao et al*. [2014a, 2014b]. However, in our study, this type is not specifically distinguished and is regarded as a normal PAD. At *L*=3.3, the *n* value is extremely high (*n*=9.1). As shown by *Gannon et al*. [2007], such steep PADs are common near the plasmapause for 157 keV. The sharply peaked PAD is also present for 350 keV electrons as shown in Figure 2. All three cases shown in the last column indicate poor fittings with SDn > 0.2 which are discarded from the subsequent statistical survey.

Figures 3 to 6 show the results of the *n* values and $\log_{10}(J)$ obtained from the analysis of the 31-month data corresponding to four electron energies, i.e., 100, 200, 350 and 1000 keV, respectively. The superimposed white lines give the estimated location of the plasmapause based on the model of *Carpenter and Anderson* [1992]: $Lpp = 5.6 - 0.46Kp^*$, where Kp* is the maximum value of the Kp index in the previous 24 h. The black area below the white curves indicates the slot region which is energy dependent at the lower energy channels. Note that some part of the black area may result from the data gap, for example, from 22 May 2013 to 17 February 2014 above *L*=3 at 100 and 200 keV. As pointed out by *Fennell et al*. [2014], no electrons with energy higher than 900keV are observed with equatorial fluxes above the background noise level in the inner zone, so that no data exist in the inner belt for 1MeV. As shown in Figure 3 to Figure 5, the PADs in the outer radiation belt and inner belt are distinctly different. For the lower energies (100, 200 and 350 keV) *n* values are mostly less than 1.5 in the outer radiation belt in the region from *L* = 6 to the inner edge of the outer belt. In contrast, inside the inner belt, *n* values are rarely less than 2. This strong distinction between the *n* values for the outer and inner belt is consistent with previous studies (e.g., *Vampola* [1998], *Gannon et al.*, 2007 and *Zhao et al.* [2014]).

A clear feature is the occurrence of high *n* values near the plasmapause, which was also reported by *Gannon et al.* [2007] for 157 keV electrons. Since this feature appears to correlate with, and remain inside of, the minimum plasmapause boundary, *Gannon et al.* [2007] suggested that pitch angle scattering by plasmaspheric hiss could be a possible explanation. Comparing the pitch angle distributions at 100, 200 and 350 keV, we find that the high *n* values mainly exist at the outer edge of the inner belt and slot region accompanying low energy fluxes. The small values of electron flux are easily captured from the bottom panels of the figures (i.e., the results of $\log_{10}(J)$), specifically around *L* = 3.5 for 100 keV, *L* = 3.0 for 200 keV and *L* = 2.7 for 350 keV, respectively. *Lyons et al.* [1972] predicted that the interaction between plasmaspheric hiss waves and electrons leads to a bump near 90°. *Lyons and Williams*

[1975] showed that injections during major storms result in electron pitch angle distributions and radial profiles that are greatly distorted from their quiet time equilibrium structure. *Zhao et al.* [2014b], by investigating an event in detail, found that inward radial diffusion may lead to the formation of a steep PAD at the beginning of the injection. While during the decay period, plasmaspheric hiss scattering plays an important role in shaping the steep PADs in the slot region and inner belt [e.g., *Thorne et al.*, 2013; *Ni et al.*, 2013]. Thus, the injection of outer belt electrons and consequent inward radial diffusion and hiss scattering can lead to the structure of peaked PADs. According to *Li et al.* [2006], the innermost plasmapause indicates the inner edge of outer radiation belt. The position of the plasmapause roughly gives the location where the outer belt MeV electrons can reach. From Figure 3 to Figure 5, it can be seen that the spatial structure and the steepness of the PADs respond differently at the specific three energies. At 100 keV, steep PADs almost fill the slot region due to the injection of outer belt electrons, while at 200 and 350 keV the steep PADs tend to restrict to the inner belt and weaken with increasing energy. Since the inner radiation belt extends to higher *L*-shell at lower energies, the outer edge of the inner belt is more vulnerable to the intrusion of the outer belt electrons. It can be seen that even weak magnetic activity would enhance the *n* values at the outer edge of the inner belt at 100keV. In the slot region and inner belt, following storms it takes a period of several days for PADs to return to their prestorm shape [*Lyons and Williams*, 1975]. Due to the constant injection (over an interval of, say, several days) of outer belt electrons into the inner belt, the steep PADs become a common structure in the slot region for

100keV. When the Kp index is so large that the innermost plasmapause reaches the core of the inner belt, the strong injection of high fluxes overwhelm the electrons at the outer edge of the inner belt, as typified by the small flux. The large *n* values are then superseded by the small *n* values that characterize strong electron flux. Since inside the inner belt the flux is also strong, the injection does not change the *n* values in this region significantly. In contrast, for higher energies (200 and 350 keV) the slot region extends over a broader range of *L* shells, therefore the inner belt is not so vulnerable to the intrusion of outer belt electrons. A higher Kp index is then needed to affect the *n* values at the outer edge of the inner belt. We also see a reduction of *n* values for much higher Kp index at 350 keV. The high *n* values at 350 keV tend to decay during quiet times, but this is not apparent at 100 keV. Hence, the reason why the high *n* values always exist near the plasmapause at 100 keV can be that the constant injection of outer radiation belt electrons and consequent inward radial diffusion and particle scattering by hiss waves sustains very strongly peaked pitch-angle distributions. At higher energies (200 and 350 keV), due to weaker injection, the features of high *n* value structures are not so strong.

To investigate the MLT and magnetic activity dependence of PADs, we calculated averaged *n* values in the *L*-MLT domain at 100, 200, 350 keV and 1MeV for three geomagnetic conditions. That is, as shown in Figure 7, we chose (from left to right) geomagnetically quiet, moderate, and active times parameterized by the Kp indices for the 31-month period. At 100keV, during quiet times (Kp < 2), large *n* values are distributed around *L*=3.8, the location of the outer edge of the inner belt. Since the plasmapause position reaches lower *L*-shells for large Kp indices, the peak of the averaged *n* values tends to be dominated by the injection of outer belt electrons. Therefore, the peak values are relatively small for 2 < Kp < 4, and the strong peak vanishes under the disturbed condition with Kp > 4. At 200 and 350 keV, the steep PADs exist around *L*=3.2 and *L*=2.8, respectively. The steepness of the PADs also attenuates with increments in Kp index. However, when the separation between the outer belt and inner belt is relatively large, the injected electrons cannot easily reach the inner belt, resulting in that the peaks in *n* values do not vanish completely at 200 and 350keV.

The steep PADs show a certain MLT dependence with larger values of averaged *n* on the dayside. Most recently, a statistical survey of plasmaspheric hiss based on the measurements from the Van Allen Probes [*Li et al.*, 2015] shows that the hiss wave intensities predominate on the dayside. The relatively intense hiss may be responsible for the steeper PADs on the dayside [e.g., *Ni et al.*, 2013, 2014].

In the outer belt, the dependence of the PAD coefficient *n* on MLT, Kp and *L*-shell is also clear. The *n* values increase with increasing Kp index, especially at noon. With decreasing *L*, the variation in the *n* values tends to weaken in response to increase in Kp. The MLT dependence is more evident at larger energies and for higher Kp index. These features are consistent with the detailed statistical results of PADs at *L*=6.0 and *L*=6.6 by *Gu et al.* [2011].

In the inner belt, there is no strong dependence of the *n* values on MLT. We calculated the averaged *n* values inside the inner belt at $L = 2.0 \pm 0.1$ as a function of MLT for

100, 200 and 350keV, the results of which are shown in Figure 8. The PADs exhibit a weak dependence on MLT, with a small peak around 12 MLT for all three energies. It can be also seen that the *n* values increase with increasing electron energy at *L*=2.0.

Figure 9 shows the averaged *n* values with an error bar, as a function of *L*-shell at five different energies for Kp < 2, 2 < Kp < 4, Kp > 4 and also for all Kp indices. At *E*=100keV, the peak of the averaged *n* values is about 9 for Kp < 2 at *L*=3.8. As Kp grows, the peak value of *n* decreases to 6 at *L*=3.4 for 2 < Kp < 4, and almost vanishes for Kp > 4. With increasing energy, the inner belt shrinks to lower *L*-shell, and as a consequence, the peak of the *n* values moves to lower *L*-shell, e.g., *L* = 3.0 at 200 keV, *L* = 2.8 at 350 keV and *L* = 2.5 at 600 keV. Different from the case of 100 keV, at 350keV, the peak *n* values still exist around L = 2.5 for Kp > 4, since the particle injection is not strong enough to reach inside of the inner belt. Thus the *n* values at the outer edge of the inner belt are not strongly affected by the injections.

Inside the inner belt, the averaged *n* values increase slightly with Kp index at *L*=2.0 for the lower energies, i.e., 100, 200 and 350 keV.

4. Conclusions

Based on the data from the Magnetic Electron Ion Spectrometer (MagEIS) instrument onboard the Van Allen Probes during the period from 1 October 2012 to 1 May 2015, a statistical analysis of the energetic radiation belt electron pitch angle distributions (PADs) has been performed. By fitting the measured pitch angle distributions with a power-law function of the sine of the local pitch angle, the power law index *n* is quantified as a function of electron kinetic energy, MLT interval, and geomagnetic index Kp. The main conclusions are summarized as follows:

1. At the outer edge of the inner belt radiation belt energetic electrons primarily present a steep distribution (corresponding to a large *n* value) at lower energies (below 700 keV). This can be caused by the injection of outer belt electrons that severely affect the PADs of energetic electrons that initially have low values of flux.

2. The steep distributions at 90° pitch angle are dependent on electron energies, geomagnetic activity and MLT. The *L*-value of these structures decreases with increasing energy since the structures lie at the outer edge of the inner belt. The strength of the magnetic activity and the distance between the inner and outer belt (which depends on energy) determine whether the injection of outer belt electrons can reach or at least approach the inner belt. Together with the effects of wave-particle interactions and radial transport, the injection modifies the electron distributions in the slot region and the outer edge of the inner belt [*Zhao et al.*, 2014b]. With increasing Kp index, the averaged *n* values of the steep PADs decrease and their location shifts to lower *L*-shells. The night-side PADs of these structures are flatter than on the dayside.

3. The pitch angle distributions in the outer belt from $L = 4$ to $L = 6$ also show considerable dependence on electron energy, geomagnetic activity and MLT. The PAD coefficient *n* is higher on the dayside compared to the nightside, which becomes more pronounced when the geomagnetic activity intensifies and electron energy increases. This feature is consistent with the analysis of PADs near the geostationary orbit using

CRRES observations [*Gu et al.*, 2011]. In addition, the *n* values on the dayside decrease with decreasing *L*-shell.

4. In the inner belt, the PADs are weakly dependent on MLT, while the PAD coefficient *n* reaches relatively high values around 12 MLT.

AcknowledgementsThis work is supported by a Discovery Grant to D.S. from the Natural Sciences and Engineering Research Council of Canada. BN thanks the support from the NSFC grants 41204120 and 41474141, the Fundamental Research Funds for the Central Universities grant 2042014kf0251, and the Project supported by the Specialized Research Fund for State Key Laboratories. All electron data analyzed in this study are obtainede from the MagEIS instrument via the website http://www.rbsp-ect.lanl.gov/science/DataDirectories.php.

References

Blake, J. B., et al. (2013), The Magnetic Electron Ion Spectrometer (MagEIS) instruments aboard the radiation belt storm probes (RBSP) spacecraft, *Space Sci. Rev.*, *179*, 383 – 421, doi:10.1007/s11214-013-9991-8.

Carbary, J. F., D. G. Mitchell, C. Paranicas, E. C. Roelof, S. M. Krimigis, N. Krupp, K. Khurana, and M. Dougherty (2011), Pitch angle distributions of energetic electrons at Saturn, *J. Geophys. Res.*, *116*, A01216, doi:10.1029/2010JA015987.

Carpenter, D. L., and R. R. Anderson (1992), An ISEE/whistler model of equatorial electron density in the magnetosphere, *J. Geophys. Res.*, *97*(A2), 1097–1108, doi:10.1029/91JA01548.

Chen, Y., R. H. W. Friedel, M. G. Henderson, S. G. Claudepierre, S. K. Morley, and H. Spence (2014), REPAD: An empirical model of pitch angle distributions for energetic electrons in the Earth's outer radiation belt, *J. Geophys. Res. Space Physics*, *119*, 1693–1708, doi:10.1002/2013JA019431.

Fennell, J. F., S. G. Claudepierre, J. B. Blake, T. P. O'Brien, J. H. Clemmons, D. N. Baker, H. E. Spence, and G. D. Reeves (2015), Van Allen Probes show that the inner radiation zone contains no MeV electrons: ECT/MagEIS data, *Geophys. Res. Lett.*, *42*, 1283–1289, doi:10.1002/2014GL062874.

Gannon, J. L., X. Li, and D. Heynderickx (2007), Pitch angle distribution analysis of radiation belt electrons based on Combined Release and Radiation Effects Satellite

Medium Electrons A data, *J. Geophys. Res.*, *112*, A05212, doi:10.1029/2005JA011565.

Gu, X., Z. Zhao, B. Ni, Y. Shprits, and C. Zhou (2011), Statistical analysis of pitch angle distribution of radiation belt energetic electrons near the geostationary orbit: CRRES observations, *J. Geophys. Res.*, *116*, A01208, doi:10.1029/2010JA016052.

Horne, R. B., N. P. Meredith, R. M. Thorne, D. Heynderickx, R. H. A. Iles, and R. R. Anderson (2003), Evolution of energetic electron pitch angle distributions during storm time electron acceleration to megaelectronvolt energies, *J. Geophys. Res.*, 108(A1), 1016, doi:10.1029/2001JA009165.

Li, X., D. N. Baker, T. P. O'Brien, L. Xie, and Q. G. Zong (2006), Correlation between the inner edge of outer radiation belt electrons and the innermost plasmapause location, *Geophys. Res. Lett.*, *33*, L14107, doi:10.1029/2006GL026294.

Li, W., Q. Ma, R. M. Thorne, J. Bortnik, C.A.Kletzing,W. S. Kurth,G. B.Hospodarsky, and Y. Nishimura (2015), Statistical properties of plasmaspheric hiss derived from Van Allen Probes data and their effects on radiation belt electron dynamics, *J. Geophys. Res. Space Physics*, *120*, doi:10.1002/2015JA021048.

Lyons, L. R., and D. J. Williams (1975), The storm and poststorm evolution of energetic (35–560 keV) radiation belt electron distributions, *J. Geophys. Res.*, *80*(28), 3985–3994.

Lyons, L. R., R. M. Thorne, and C. F. Kennel (1972), Pitch-angle diffusion of radiation belt electrons within the plasmasphere, *J. Geophys. Res.*, *77*(19), 3455–3474.

Mauk, B. H., N. J. Fox, S. G. Kanekal, R. L. Kessel, D. G. Sibeck, and A. Ukhorskiy (2012), Science objectives and rationale for the Radiation Belt Storm Probes mission, *Space Sci. Rev.*, 1–15, doi:10.1007/s11214-012-9908-y.

Ni, B., J. Bortnik, R. M. Thorne, Q. Ma, and L. Chen (2013), Resonant scattering and resultant pitch angle evolution of relativistic electrons by plasmaspheric hiss, *J. Geophys. Res. Space Physics*, 118, 7740-7751, doi:10.1002/2013JA019260.

Ni, B., W. Li, R. M. Thorne, J. Bortnik, Q. Ma, L. Chen, C. Kletzing, W. Kurth, G. Hospodarsky, G. Reeves, H. Spence, J. Blake, J. Fennell, and S. Claudepierre (2014), Resonant scattering of energetic electrons by unusual low-frequency hiss, *Geophys. Res. Lett.*, 41, 1854-1861, doi:10.1002/2014GL059389.

Ni, B., Z. Zou, X. Gu, C. Zhou, R. M. Thorne, J. Bortnik, R. Shi, Z. Zhao, D. N. Baker, S. G. Kanekal, et al. (2015), Variability of the pitch angle distribution of radiation belt ultrarelativistic electrons during and following intense geomagnetic storms: Van Allen Probes observations, *J. Geophys. Res. Space Physics, 120*, doi:10.1002/2015JA021065.

Sibeck, D. G., R. W. McEntire, A. T. Y. Lui, R. E. Lopez, and S. M. Krimigis (1987), Magnetic field drift shell splitting: Cause of unusual dayside particle pitch angle distributions during storms and substorms, *J. Geophys. Res.*, *92*(A12), 13,485 – 13,497, doi:10.1029/JA092iA12p13485.

Spence, H. E., et al. (2013), Science goals and overview of the Energetic Particle, Composition, and thermal plasma (ECT) suite on NASA's Radiation Belt Storm Probes (RBSP) mission, *Space Sci. Rev.*, *179*, 311 – 336, doi:10.1007/s11214-013-0007-5.

Summers, D., R. Tang, and R. M. Thorne (2009), Limit on stably trapped particle fluxes in planetary magnetospheres, *J. Geophys. Res.*, *114*, A10210, doi:10.1029/2009JA014428.

Summers, D., and R. Shi (2014), Limiting energy spectrum of an electron radiation belt, *J. Geophys. Res. Space Physics,119*, 6313–6326, doi:10.1002/2014JA020250.

Thorne, R. M., W. Li, B. Ni, Q. Ma, J. Bortnik, D. Baker, H. Spence, G. Reeves, M. Henderson, C. Kletzing, W. Kurth, G. Hospodarsky, D. Turner, and V. Angelopolous (2013), Evolution and slow decay of an unusual narrow ring of relativistic electrons near L ~ 3.2 following the September 2012 magnetic storm, *Geophys. Res. Lett.*, 40, 3507-3511, doi:10.1002/grl.50627.

Vampola, A. L. (1998), Outer zone energetic electron environment update, in *Proceedings of the Conference on the High Energy Radiation Background in Space*, pp. 128–136, Inst. of Electr. and Electr. Eng., New York.

West, H. I., Jr., R. M. Buck, and J. R. Walton (1973), Electron pitch angle distributions through the magnetosphere as observed on Ogo 5, *J. Geophys. Res., 78*, 1064‒1081.

Zhao, H., X. Li, J. B. Blake, J. F. Fennell, S. G. Claudepierre, D. N. Baker, A. N. Jaynes, D. M. Malaspina, and S. G. Kanekal (2014a), Peculiar pitch angle distribution of relativistic electrons in the inner radiation belt and slot region, *Geophys. Res. Lett.*, *41*, 2250–2257, doi:10.1002/2014GL059725.

Zhao, H., X. Li, J. B. Blake, J. F. Fennell, S. G. Claudepierre, D. N. Baker, A. N. Jaynes, and D. M. Malaspina (2014b), Characteristics of pitch angle distributions of hundreds of keV electrons in the slot region and inner radiation belt, *J. Geophys. Res. Space Physics*, *119*, 9543–9557, doi:10.1002/2014JA020386.

Figure Captions

Figure 1. Solar wind Bz component; solar wind speed V_{sw} and dynamic pressure P_{dyn}; Dst, Kp and AE indices from Oct 1, 2012 to May 1, 2015.

Figure 2. Examples of the PAD fitting.

Figure 3. The *n* values (top) and $\log_{10}(J)$ values (bottom) of PADs of ~100keV electrons based on the formula $f = J \sin^n\alpha$ as a function of *L*-shell from 1 October 2012 to 1 May 2015. The overlay white lines give the estimated location of the plasmapause based on *Carpenter and Anderson* [1992]: $Lpp = 5.6 - 0.46\text{Kp}^*$, where Kp* is the maximum value of the Kp index in the previous 24 h.

Figure 4. As in Figure 3 except for ~200keV electrons.

Figure 5. As in Figure 3 except for ~350keV electrons.

Figure 6. As in Figure 3 except for ~1MeV electrons.

Figure 7. Averaged PAD coefficient *n* as a function of *L* and MLT at 100keV, 200keV, 350keV and 1MeV under three geomagnetic conditions ($Kp < 2$, $2 < Kp < 4$ and $Kp > 4$).

Figure 8. The averaged *n* values in the inner belt ($L = 2.0 \pm 1$) as a function of MLT at three energies.

Figure 9. The averaged *n* values as a function of *L*-shell at 100keV, 200keV, 350keV, 600keV and 1MeV under quiet, moderate, active and all geomagnetic conditions.

Figure 1

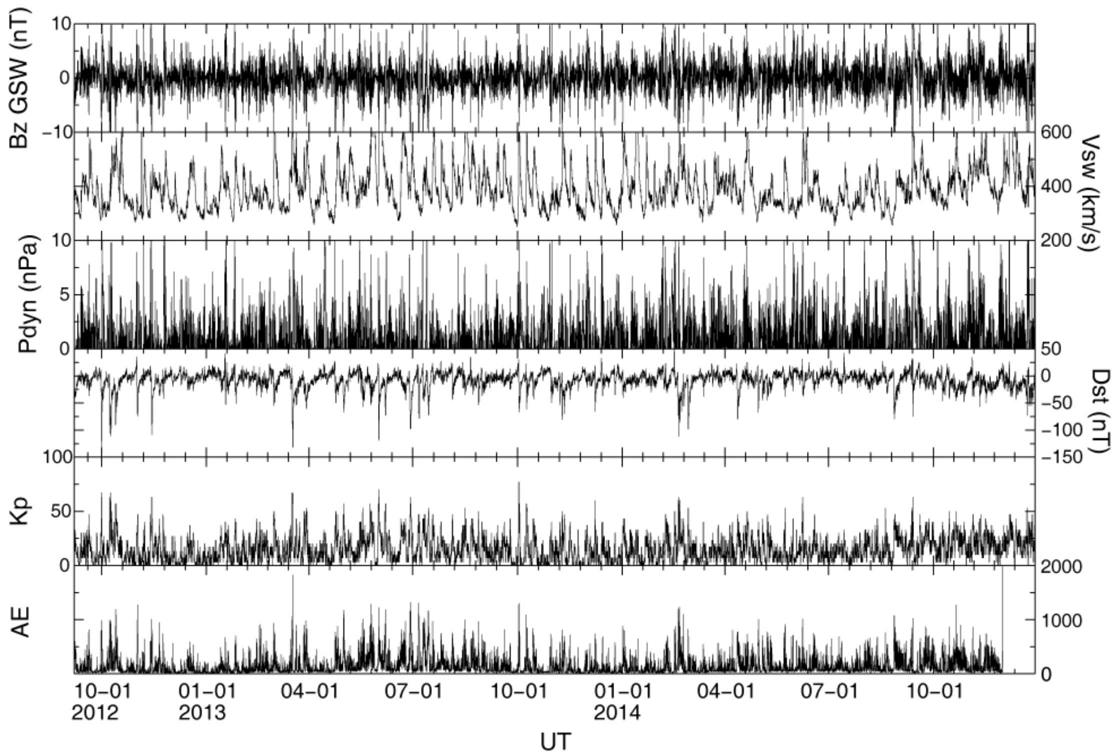

Figure 1. Solar wind Bz component; solar wind speed V_{sw} and dynamic pressure P_{dyn}; Dst, Kp and AE indices from Oct 1, 2012 to May 1, 2015.

Figure 2

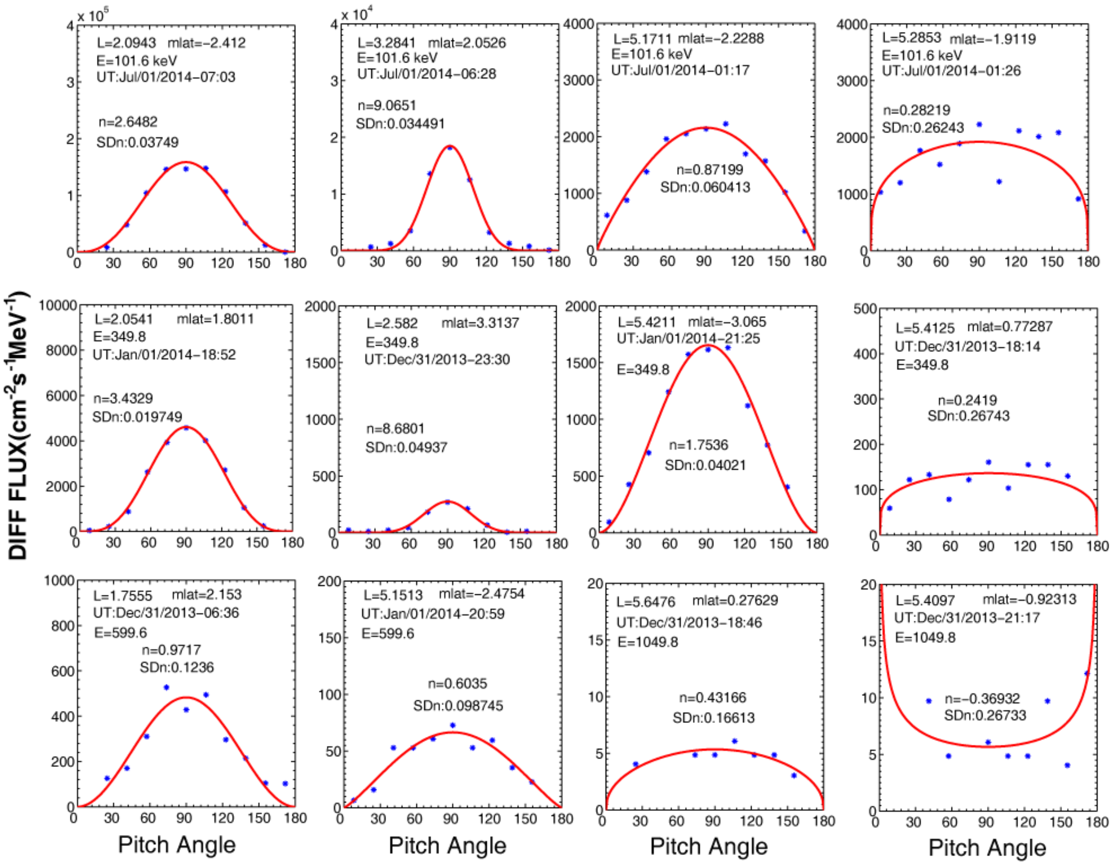

Figure 2. Examples of the PAD fitting.

Figure 3

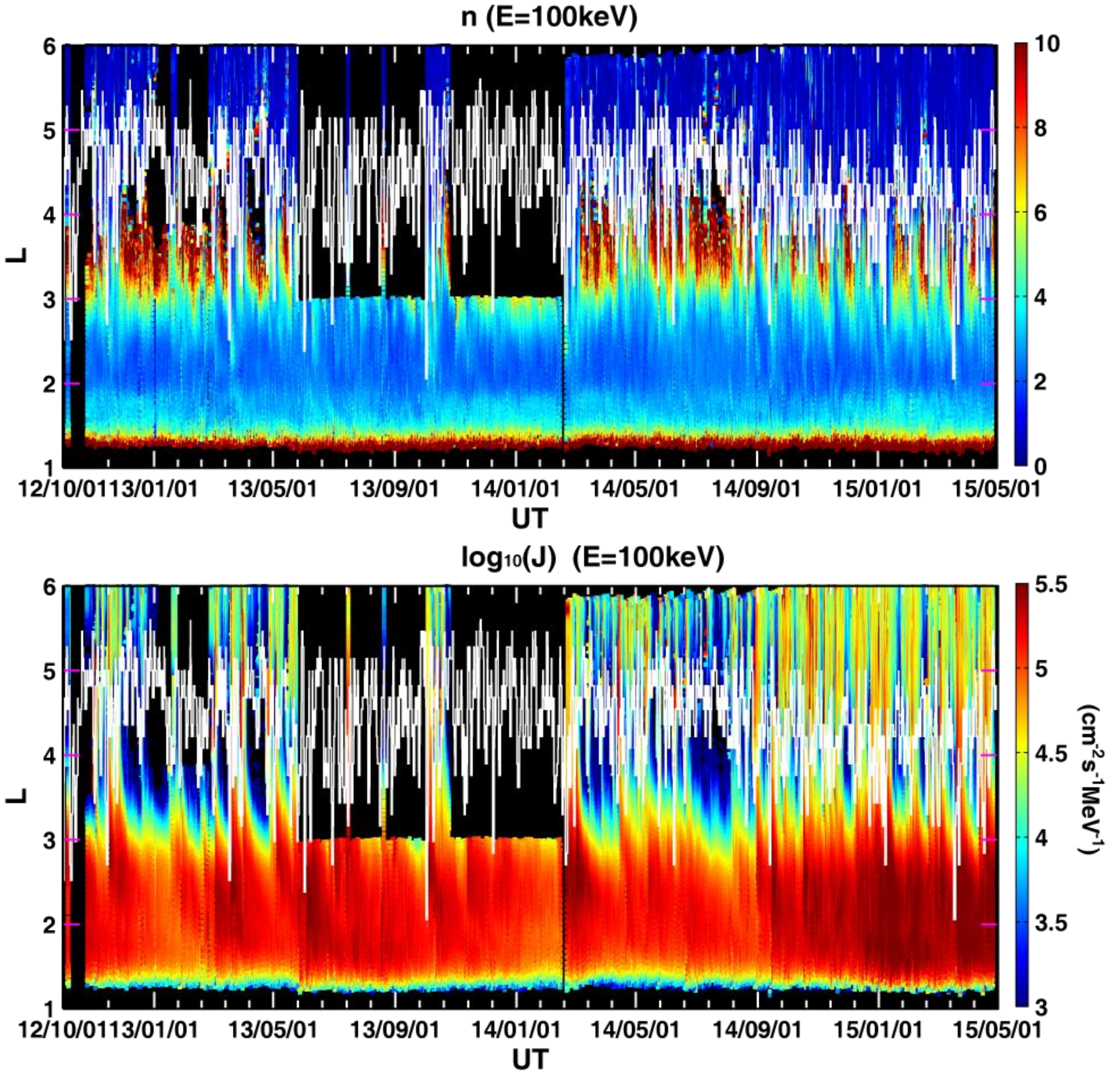

Figure 3. The *n* values (top) and $\log_{10}(J)$ values (bottom) of PADs of ~100keV electrons based on the formula $f = J \sin^n \alpha$ as a function of *L*-shell from 1 October 2012 to 1 May 2015. The overlay white lines give the estimated location of the plasmapause based on *Carpenter and Anderson* [1992]: $Lpp = 5.6 - 0.46\text{Kp}^*$, where Kp* is the maximum value of the Kp index in the previous 24 h.

Figure 4

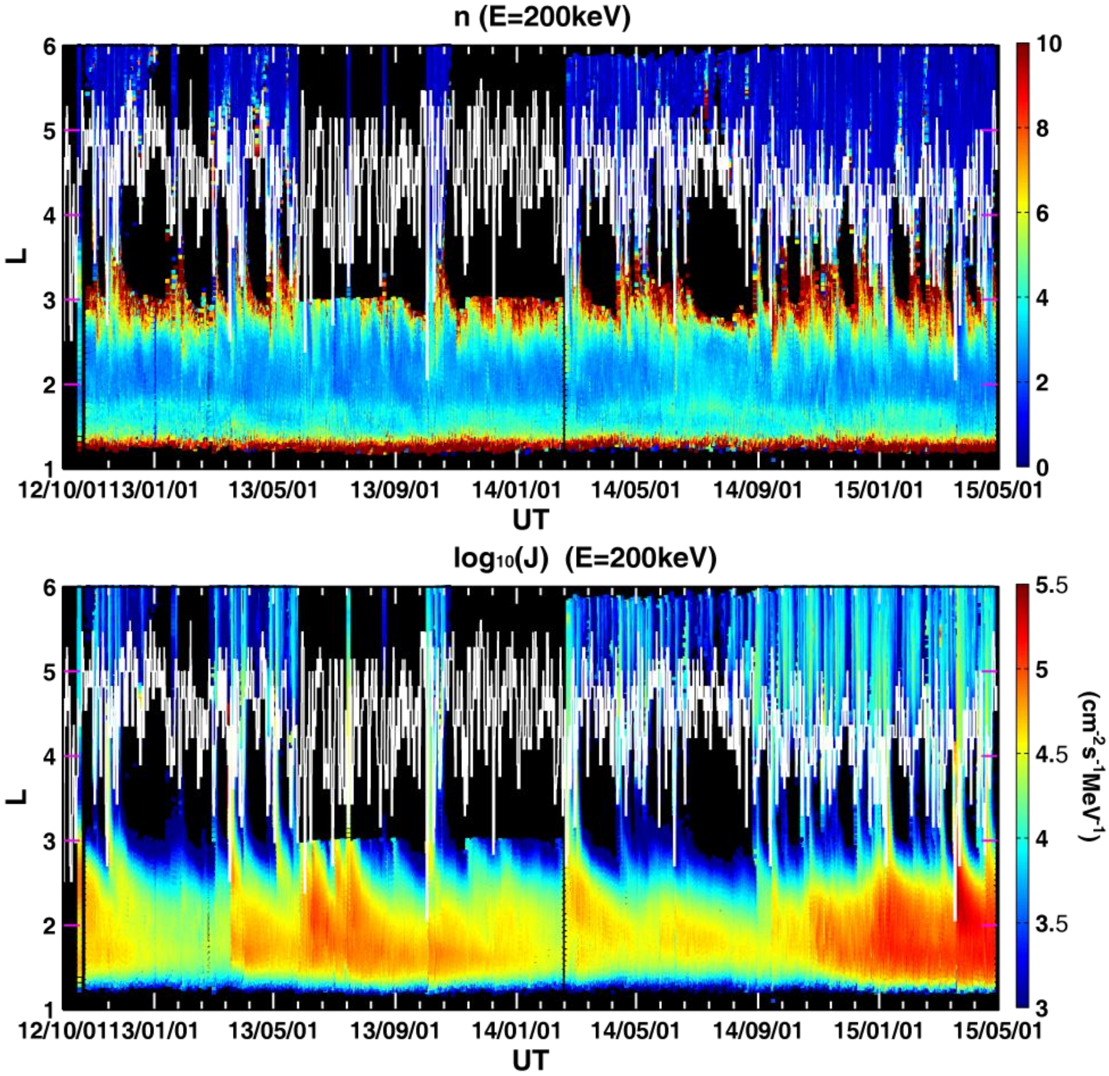

Figure 4. As in Figure 3 except for ~200keV electrons.

Figure 5

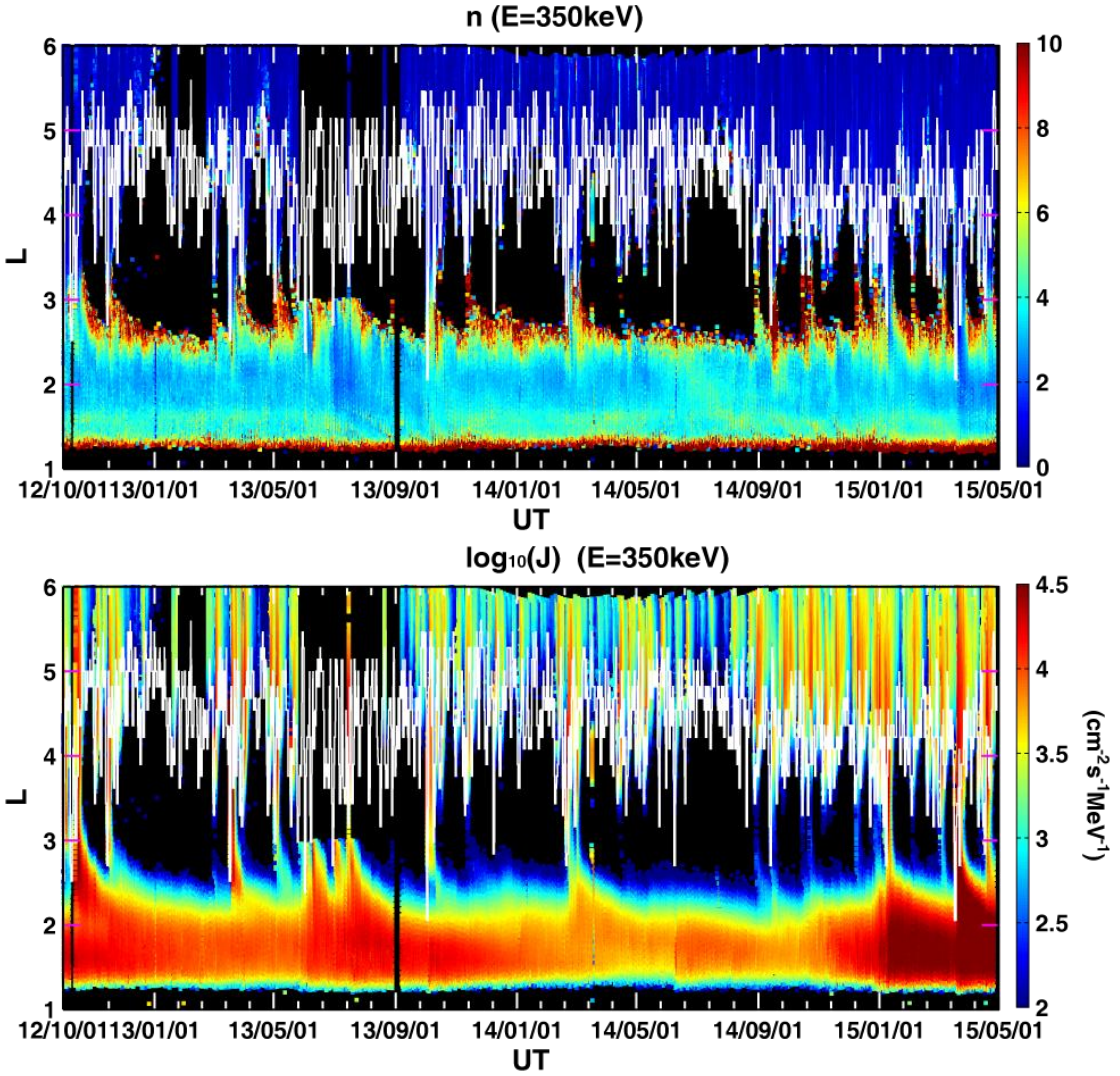

Figure 5. As in Figure 3 except for ~350keV electrons.

Figure 6

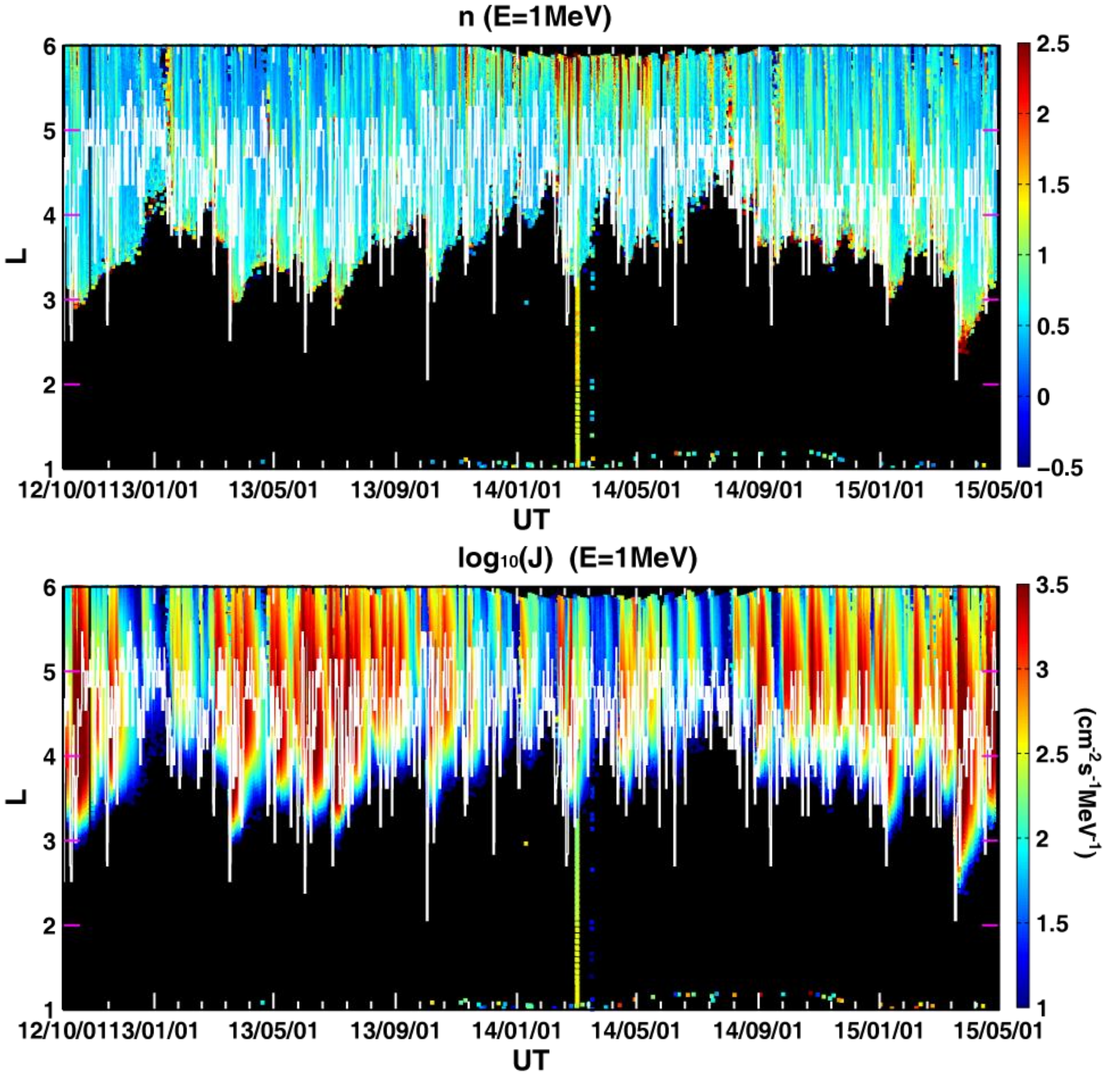

Figure 6. As in Figure 3 except for ~1MeV electrons.

435 Figure 7

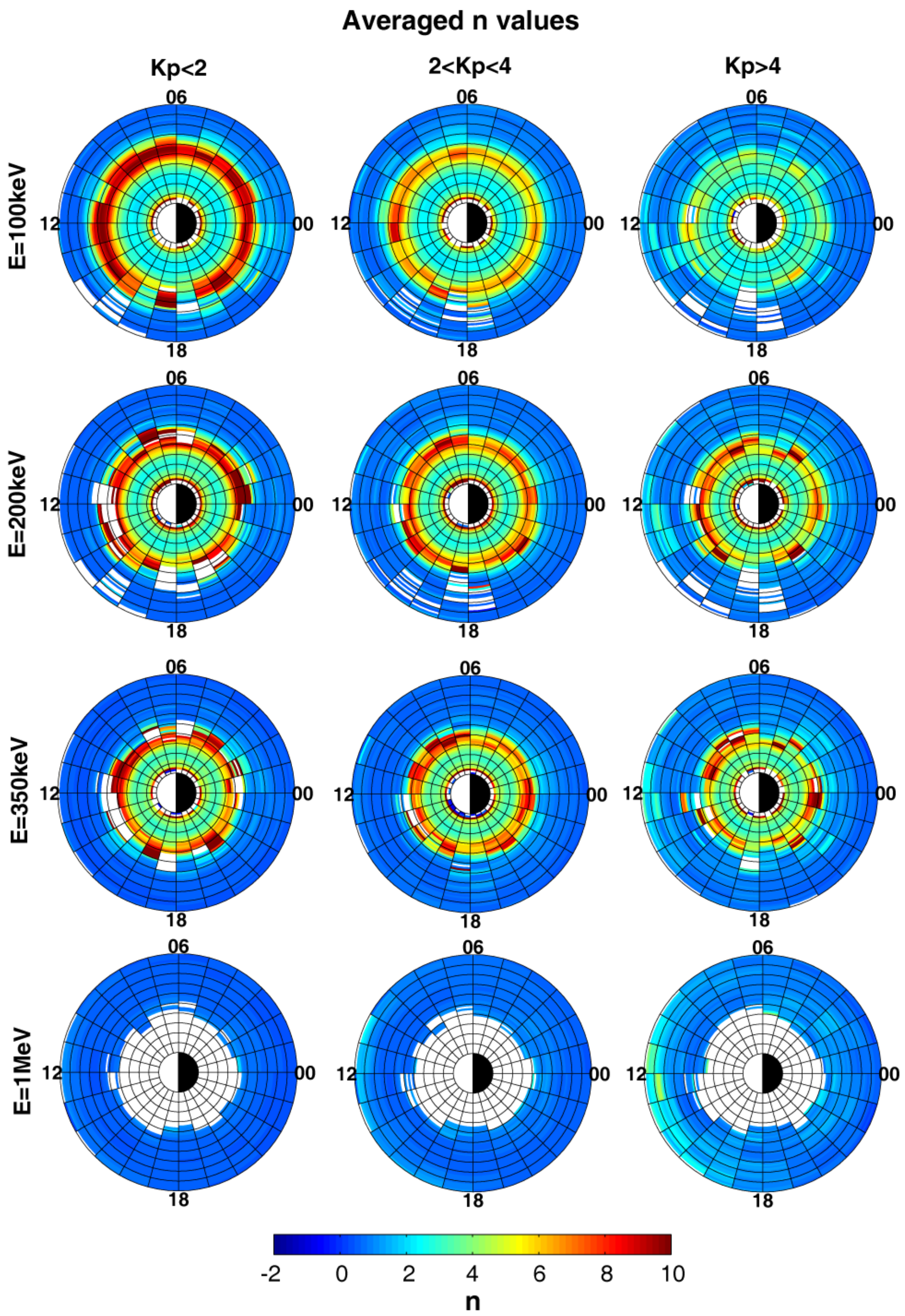

436

437 Figure 7. Averaged PAD coefficient *n* as a function of *L* and MLT at 100keV, 200keV,

438 350keV and 1MeV under three geomagnetic conditions (Kp < 2, 2 < Kp < 4 and Kp >

439 4).

Figure 8

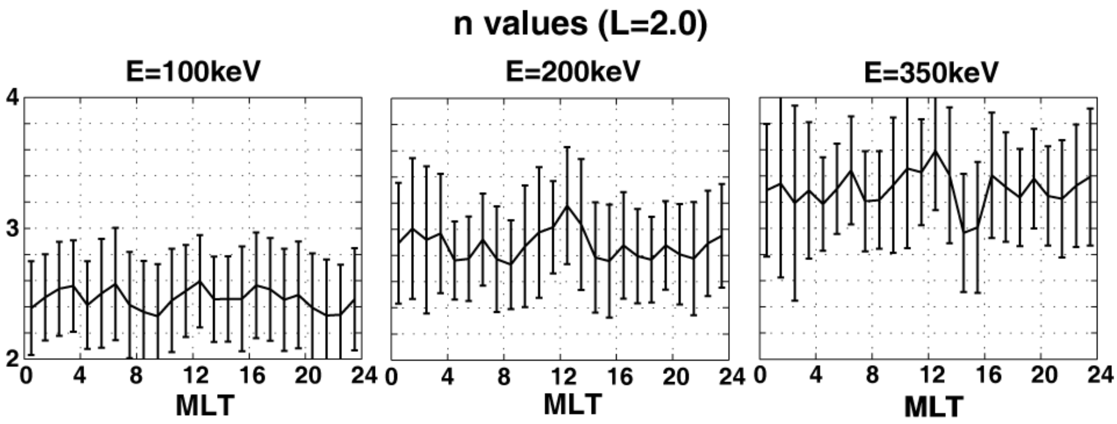

Figure 8. The averaged *n* values in the inner belt (L = 2.0 ±1) as a function of MLT at three energies.

Figure 9

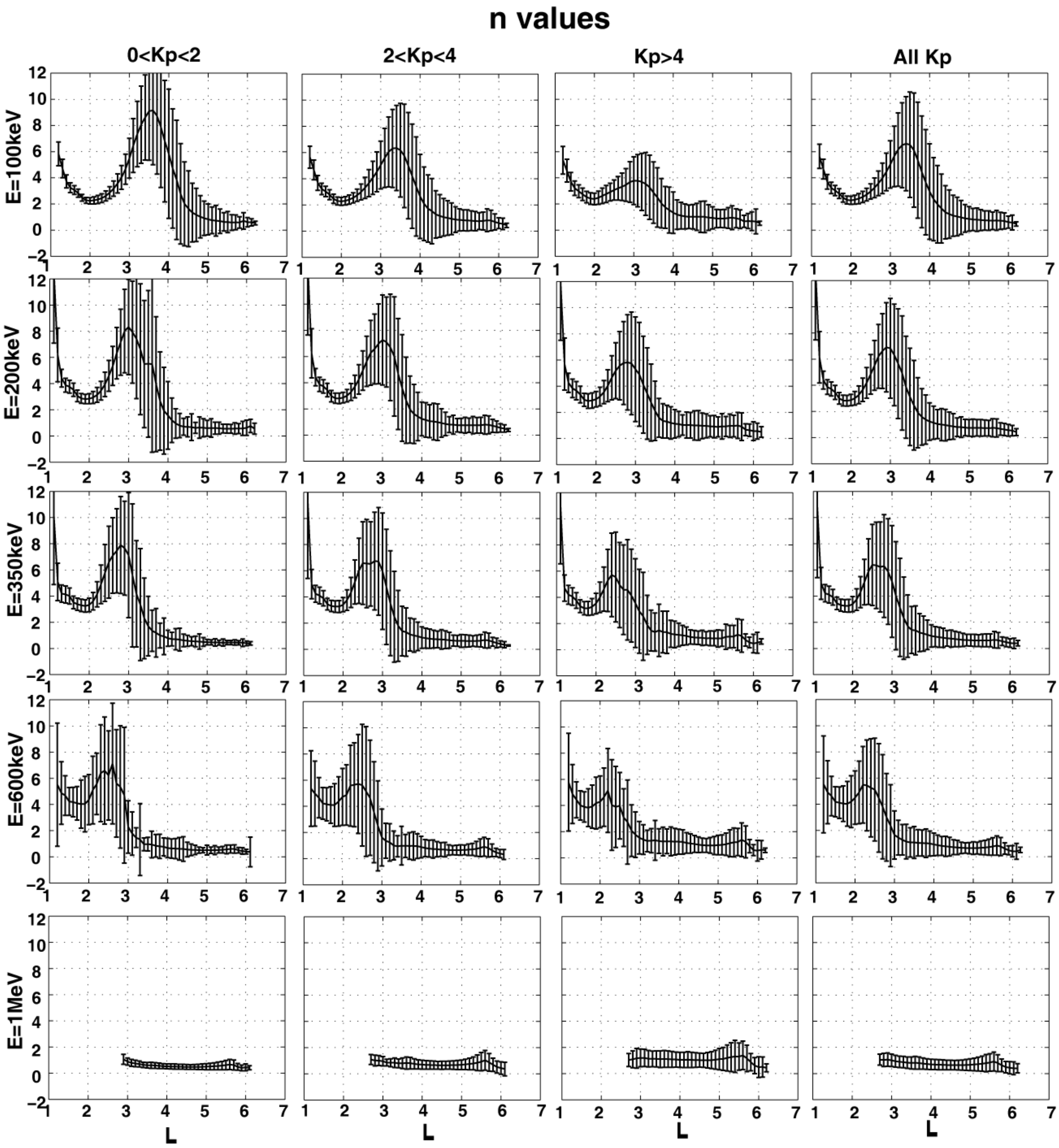

Figure 9. The averaged *n* values as a function of *L*-shell at 100keV, 200keV, 350keV, 600keV and 1MeV under quiet, moderate, active and all geomagnetic conditions.

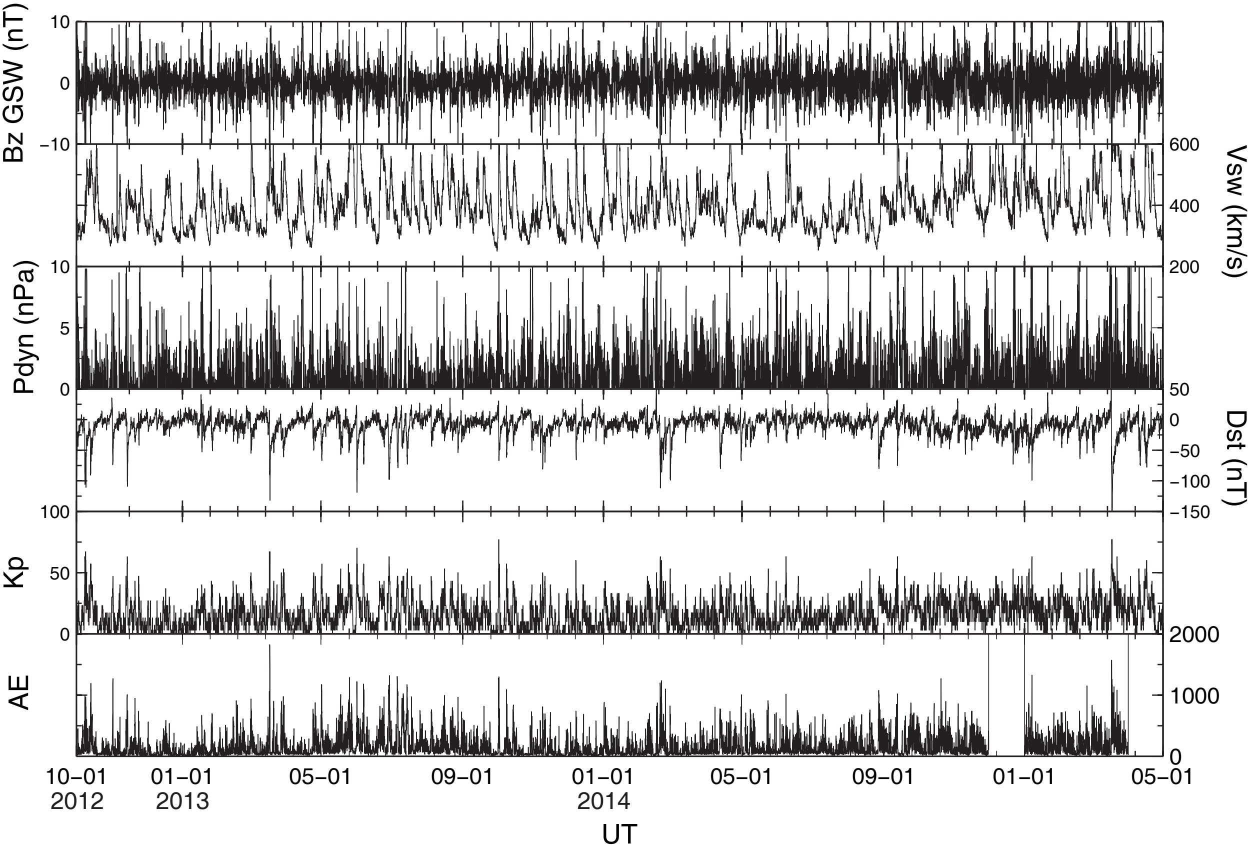
Bz GSW (nT)
10
0
−10
Vsw (km/s)
600
400
200
Pdyn (nPa)
10
5
0
Dst (nT)
50
0
−50
−100
−150
Kp
100
50
0
AE
2000
1000
0
10−01
2012
01−01
2013
05−01
09−01
01−01
2014
05−01
09−01
01−01
05−01
UT

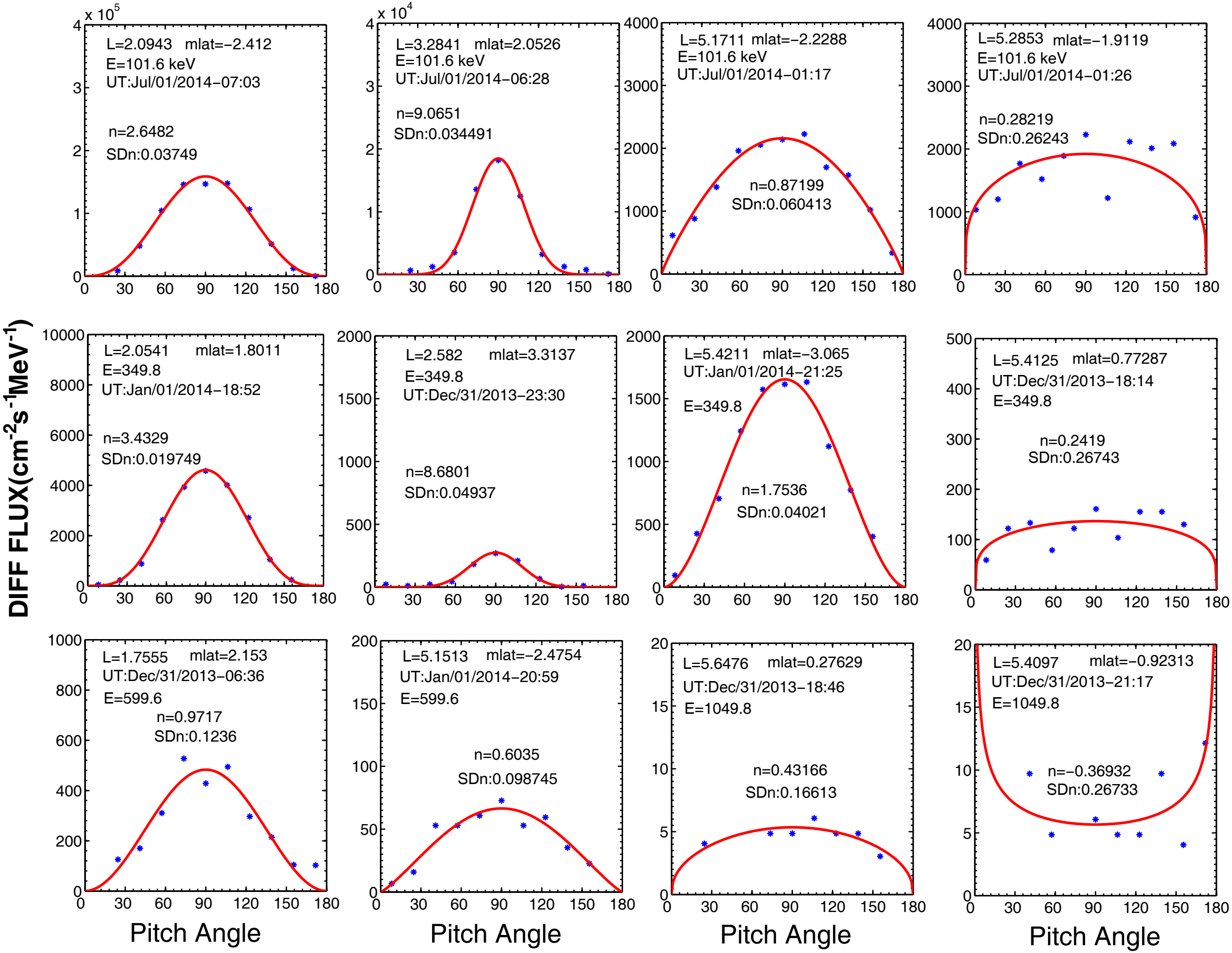

DIFF FLUX(cm-2s-1MeV-1)
Pitch Angle
L=2.0943 mlat=−2.412
E=101.6 keV
UT:Jul/01/2014−07:03
n=2.6482
SDn:0.03749
L=3.2841 mlat=2.0526
E=101.6 keV
UT:Jul/01/2014−06:28
n=9.0651
SDn:0.034491
L=5.1711 mlat=−2.2288
E=101.6 keV
UT:Jul/01/2014−01:17
n=0.87199
SDn:0.060413
L=5.2853 mlat=−1.9119
E=101.6 keV
UT:Jul/01/2014−01:26
n=0.28219
SDn:0.26243
L=2.0541 mlat=1.8011
E=349.8
UT:Jan/01/2014−18:52
n=3.4329
SDn:0.019749
L=2.582 mlat=3.3137
E=349.8
UT:Dec/31/2013−23:30
n=8.6801
SDn:0.04937
L=5.4211 mlat=−3.065
UT:Jan/01/2014−21:25
E=349.8
n=1.7536
SDn:0.04021
L=5.4125 mlat=0.77287
UT:Dec/31/2013−18:14
E=349.8
n=0.2419
SDn:0.26743
L=1.7555 mlat=2.153
UT:Dec/31/2013−06:36
E=599.6
n=0.9717
SDn:0.1236
L=5.1513 mlat=−2.4754
UT:Jan/01/2014−20:59
E=599.6
n=0.6035
SDn:0.098745
L=5.6476 mlat=0.27629
UT:Dec/31/2013−18:46
E=1049.8
n=0.43166
SDn:0.16613
L=5.4097 mlat=−0.92313
UT:Dec/31/2013−21:17
E=1049.8
n=−0.36932
SDn:0.26733

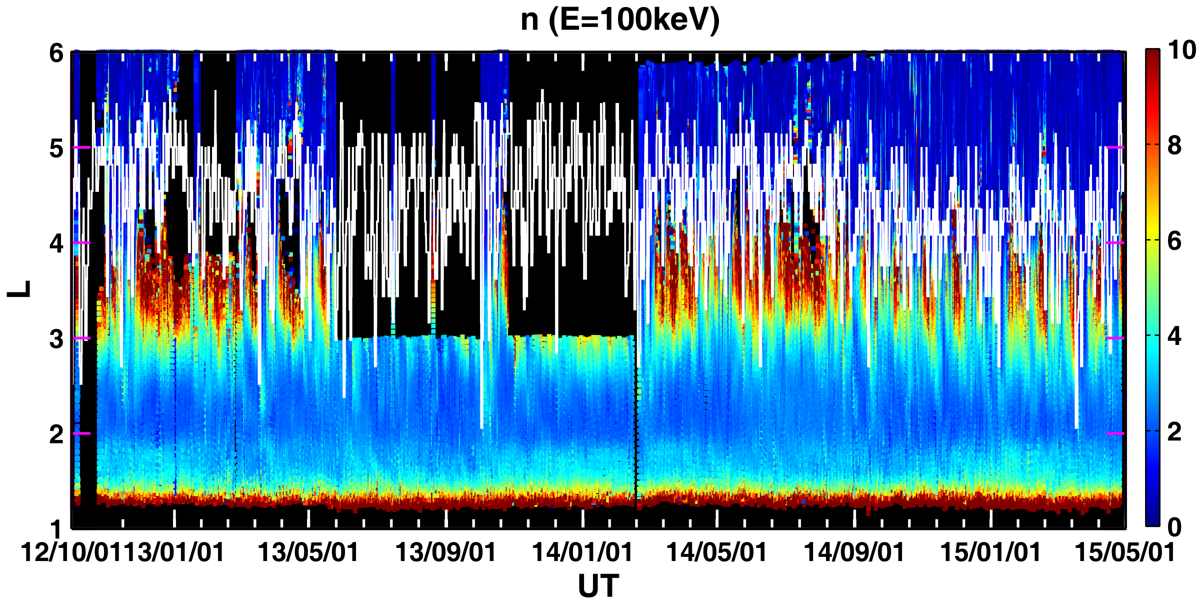
n (E=100keV)
L
6
5
4
3
2
1
12/10/01
13/01/01
13/05/01
13/09/01
14/01/01
14/05/01
14/09/01
15/01/01
15/05/01
UT
10
8
6
4
2
0

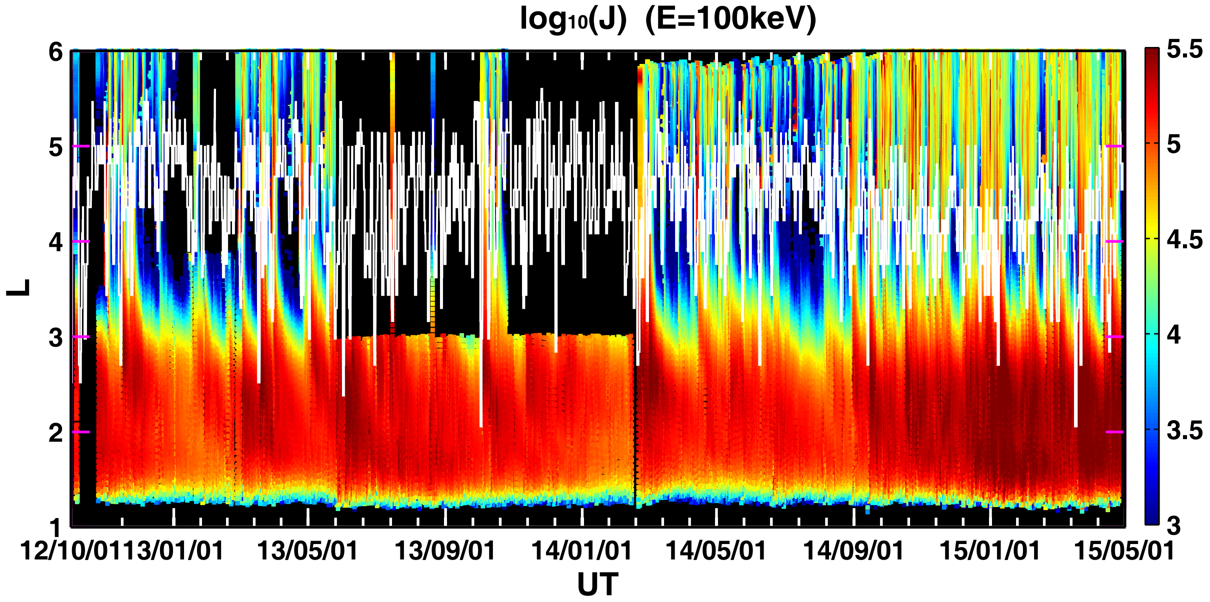

log10(J) (E=100keV)
L
6
5
4
3
2
1
12/10/01
13/01/01
13/05/01
13/09/01
14/01/01
14/05/01
14/09/01
15/01/01
15/05/01
UT
5.5
5
4.5
4
3.5
3
(cm-2s-1MeV-1)

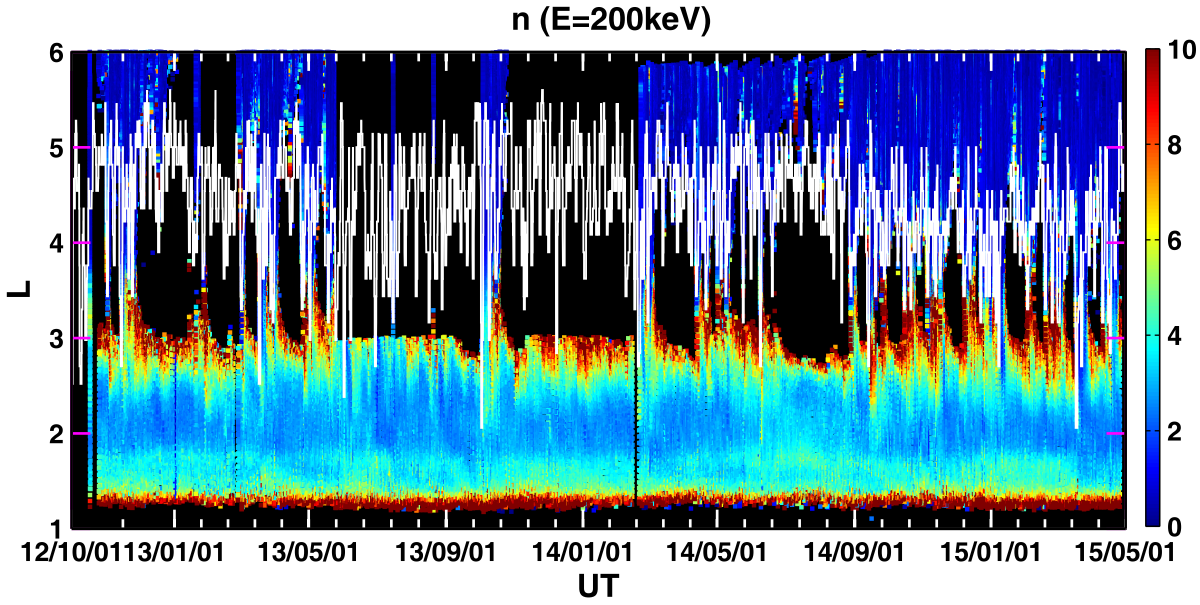

n (E=200keV)
L
6
5
4
3
2
1
12/10/01
13/01/01
13/05/01
13/09/01
14/01/01
14/05/01
14/09/01
15/01/01
15/05/01
UT
10
8
6
4
2
0

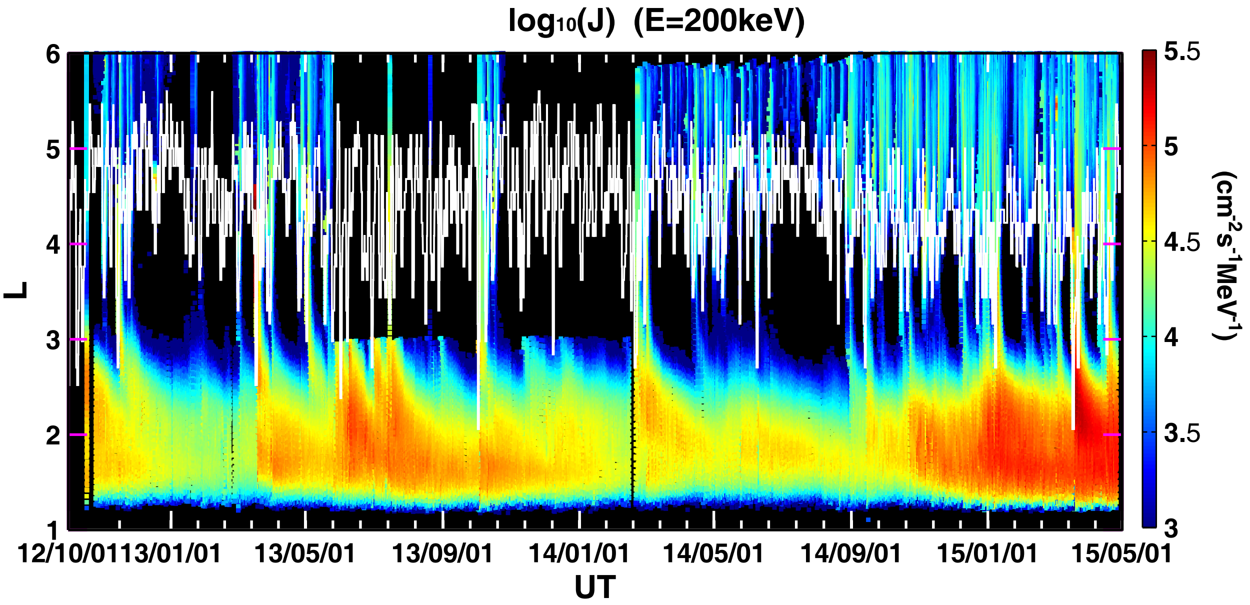
log10(J) (E=200keV)
6
5
4
3
2
1
L
12/10/01
13/01/01
13/05/01
13/09/01
14/01/01
14/05/01
14/09/01
15/01/01
15/05/01
UT
5.5
5
4.5
4
3.5
3
(cm-2s-1MeV-1)

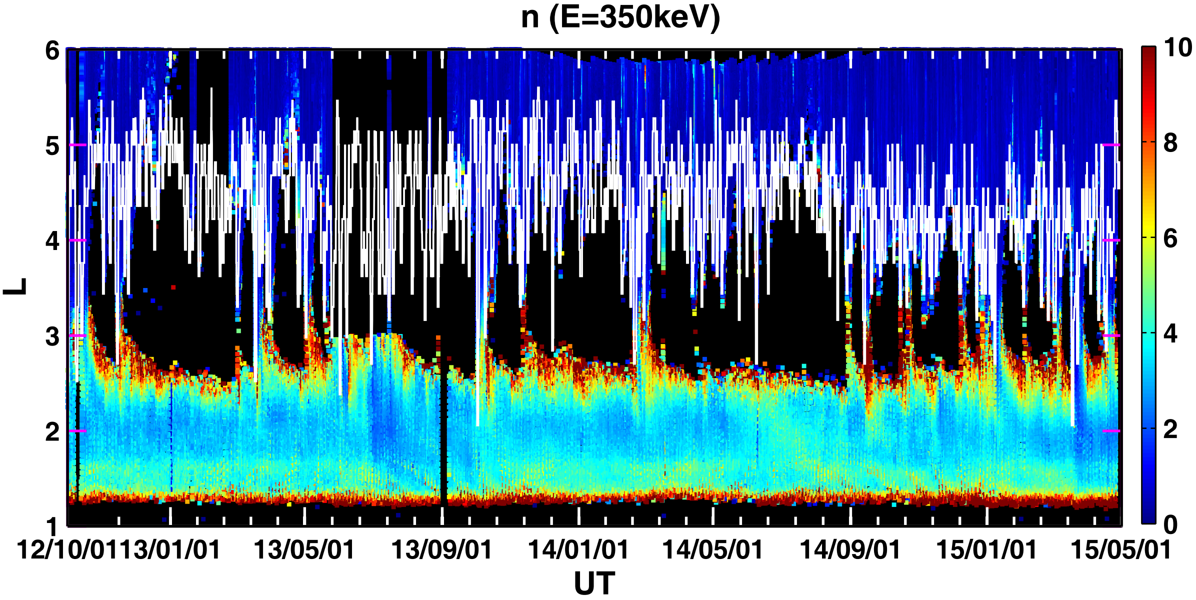

n (E=350keV)
L
UT
12/10/01
13/01/01
13/05/01
13/09/01
14/01/01
14/05/01
14/09/01
15/01/01
15/05/01
1
2
3
4
5
6
0
2
4
6
8
10

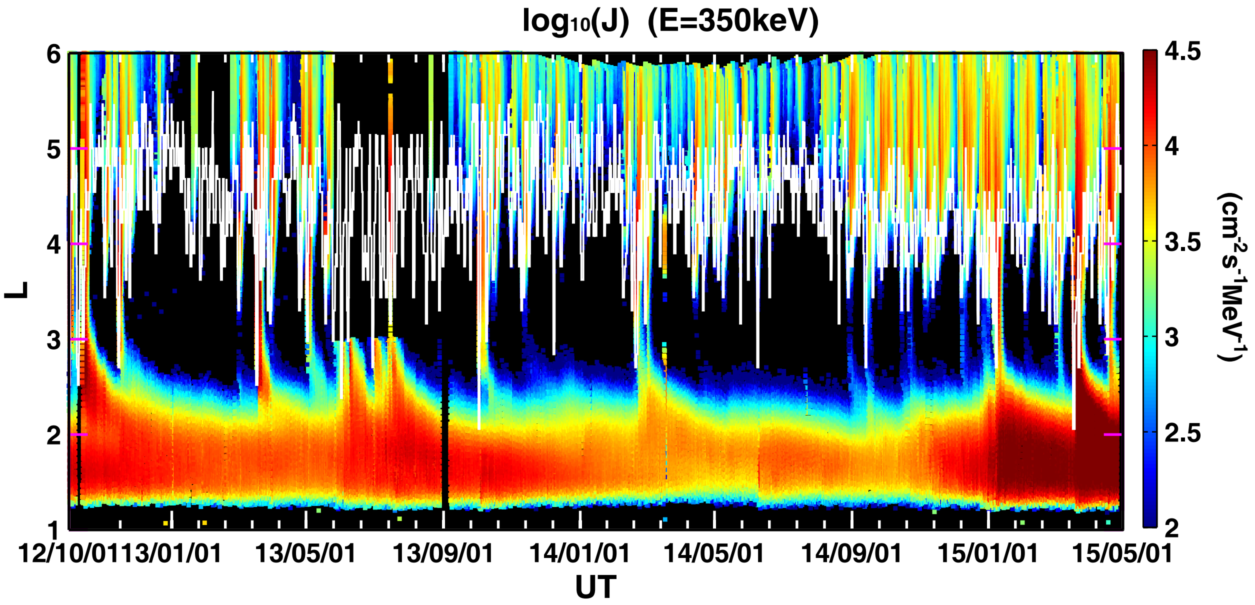

log10(J) (E=350keV)
L
6
5
4
3
2
1
12/10/01
13/01/01
13/05/01
13/09/01
14/01/01
14/05/01
14/09/01
15/01/01
15/05/01
UT
4.5
4
3.5
3
2.5
2
(cm-2s-1MeV-1)

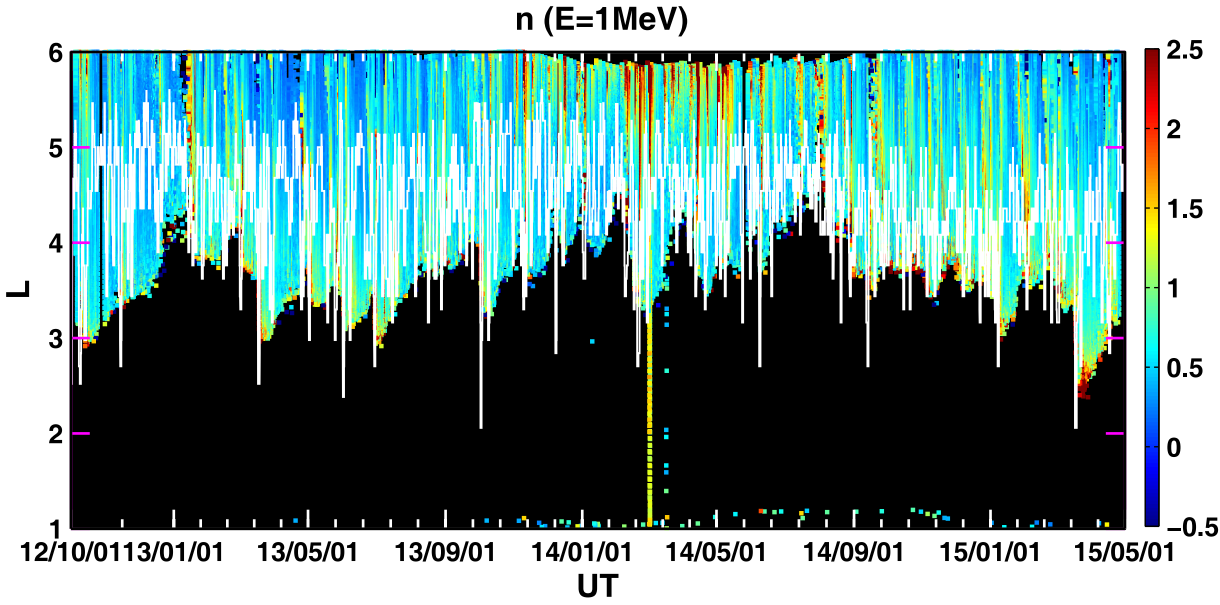
n (E=1MeV)
L
6
5
4
3
2
1
12/10/01
13/01/01
13/05/01
13/09/01
14/01/01
14/05/01
14/09/01
15/01/01
15/05/01
UT
2.5
2
1.5
1
0.5
0
−0.5

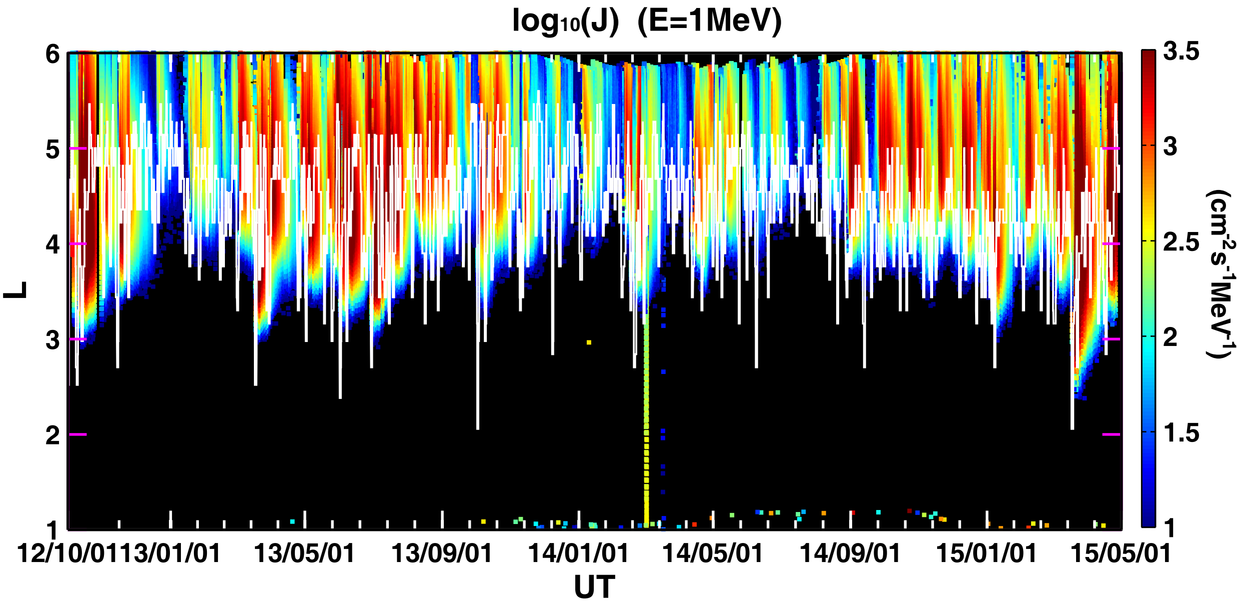

log10(J) (E=1MeV)
L
6
5
4
3
2
1
12/10/01
13/01/01
13/05/01
13/09/01
14/01/01
14/05/01
14/09/01
15/01/01
15/05/01
UT
3.5
3
2.5
2
1.5
1
(cm-2s-1MeV-1)

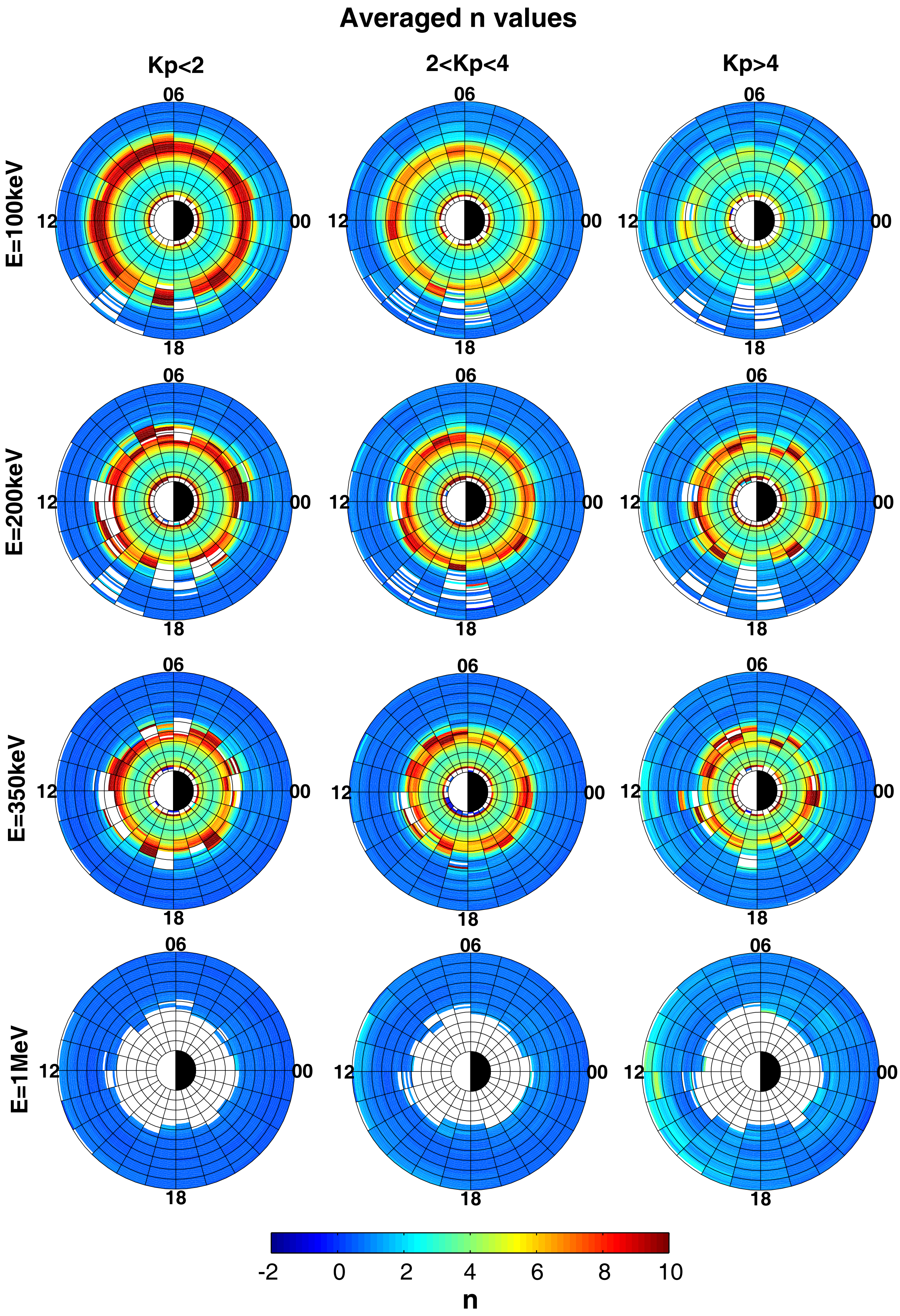
Averaged n values
Kp<2
2<Kp<4
Kp>4
E=100keV
E=200keV
E=350keV
E=1MeV
06
12
00
18
-2
0
2
4
6
8
10
n

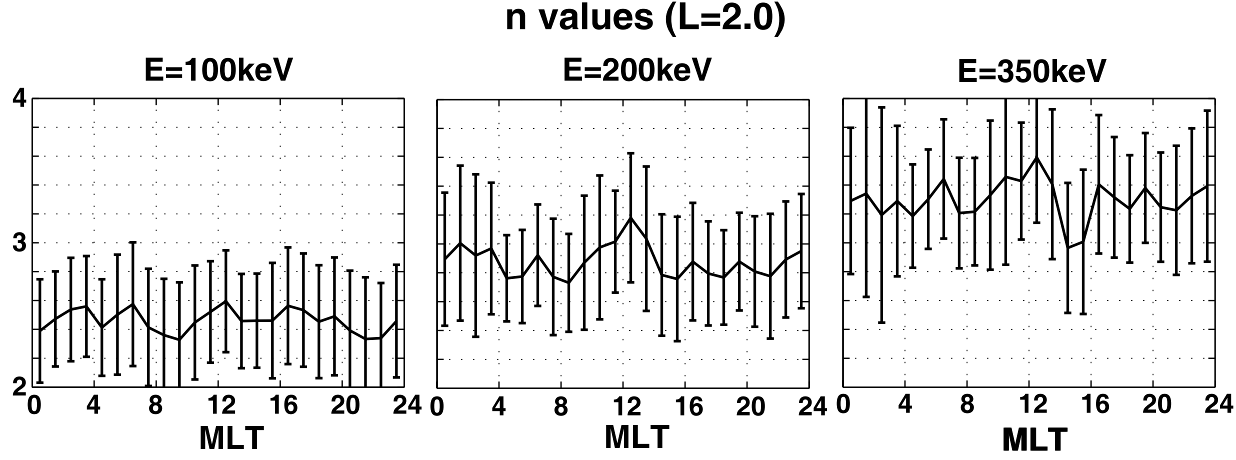
n values (L=2.0)
E=100keV
E=200keV
E=350keV
4
3
2
0
4
8
12
16
20
24
MLT
MLT
MLT

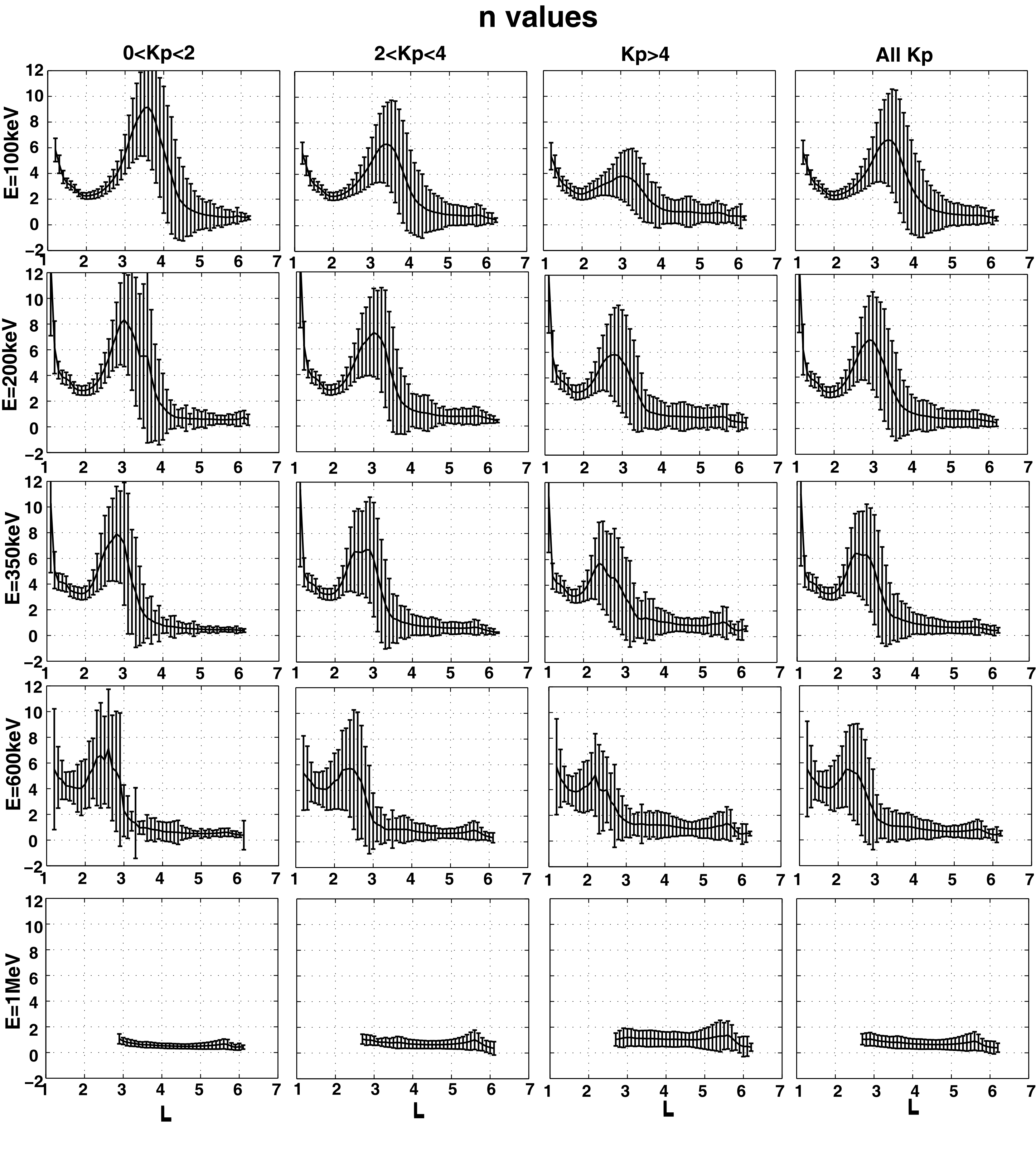
n values
0<Kp<2
2<Kp<4
Kp>4
All Kp
E=100keV
E=200keV
E=350keV
E=600keV
E=1MeV
L